



Meteorological Drivers of Extreme Swells on the Peruvian Coast

Gonzalo Agurto^{1,2}, Soledad Collazo^{2,3}, Ricardo García-Herrera^{2,3}

¹División de Meteorología Marina, Departamento de Oceanografía, Dirección de Hidrografía y Navegación, Marina de Guerra del Perú, Callao, 07021, Perú

5 ²Departamento de Física de la Tierra y Astrofísica, Facultad de Ciencias Físicas, Universidad Complutense de Madrid (UCM), Madrid, 28040, Spain

³Instituto de Geociencias (IGEO), Consejo Superior de Investigaciones Científicas–Universidad Complutense de Madrid (CSIC–UCM), Madrid, 28040, Spain

Correspondence to: Soledad Collazo (scollazo@ucm.es)

10 **Abstract.** In this study, we analyze the meteorological configurations leading to extreme ocean swells along the Peruvian coast, which are frequently produced by remote Pacific storms from both hemispheres. Using extreme-swell warnings from the Peruvian Navy and ERA5 reanalysis, we examine five austral-winter Southern Hemisphere (SH) events (very strong, south-westerly) and six boreal-winter Northern Hemisphere (NH) events (strong, north-westerly). Event-centred composites are computed over lead windows guided by estimated swell travel times (3–4 days in the SH; 8–11 days in the NH). In both
15 hemispheres, a deep extratropical cyclone becomes vertically aligned from sea-level pressure through 500 hPa to 250 hPa before coastal peak swell, while an upper-level jet core strengthens and organizes a persistent corridor of enhanced surface westerlies over the swell-generation region. In the SH, coherent surrounding ridging tightens the meridional pressure gradient and co-occurs with a strengthened, sharper polar-front jet. In the NH, preconditioning is dominated by a deep central–western North Pacific low with comparatively weak, localized ridging and a markedly intensified, more zonally extended subtropical
20 jet, while the polar-front jet weakens. A flow-analogue framework suggests a recent strengthening of SH event-related surface winds consistent with increased large-scale pressure contrasts and a shift toward more positive Southern Annular Mode conditions, whereas NH events show no robust trend and attribution is obscured by strong interannual-to-decadal variability. These results can support earlier recognition of remote swell hazards affecting Peru and, consequently, can lead to an improvement of early warning systems.

25 1 Introduction

Coastal communities worldwide are increasingly impacted by extreme wave events. These events, often referred to as coastal wave storms or anomalous swells, can result in flooding, coastal erosion, and disruptions to maritime activities. While some extreme wave conditions are generated by local storms, many destructive coastal events are driven by ocean swells originating from distant extratropical cyclones. Swell can cross ocean basins with modest attenuation (Barber and Ursell, 1948; Ardhuin
30 et al., 2009). In the Pacific, about 22% of coastal extremes originate from the opposite hemisphere (across the Equator) and



~30–35% of tropical extremes originate at higher latitudes (Boucharel et al., 2021). This underscores a strong interconnection between mid-latitude storminess and low-latitude coastal impacts, highlighting the need to account for remote wave forcing in coastal risk assessments.

The Pacific Ocean has a well-documented history of long-range swell events impacting distant shores. In particular, the Pacific
35 coasts of the Americas have experienced recently severe anomalous swell episodes triggered by remote storms. For example, an anomalous southwest swell event in May 2023 caused coastal flooding and the closure of dozens of ports in Peru (Infobae, 2023). A late-December 2024 swell event generated by a winter storm in the North Pacific impacted Peru’s northern tourist beaches and small ports, underscoring the far-reaching effects of remote storm forcing (RPP Noticias, 2024). These events caught coastal communities by surprise, illustrating how storm activity in remote regions can translate into sudden coastal
40 hazards even under fair local weather.

For this region, prior studies have noted that the most potent swell-generating storms often involve quasi-stationary or slow-moving frontal systems, which allow wind energy to accumulate. For instance, Alves (2006) identified mid-latitude cyclones as the chief source of long-period swells in the Pacific. Similarly, an analysis by Campos-Caba (2016) found that the largest swells impacting Chile and Peru were typically caused by distant storms with stalled or multi-day frontal activity over 3,000 km
45 offshore. These prolonged fetch conditions favour the production of exceptionally energetic swells.

Most “ordinary” swell events arise from midlatitude extratropical depressions following typical storm-track paths, whose sustained winds generate long-period waves that radiate far from the source (Alves, 2006; Semedo et al., 2011). By contrast, extreme swell episodes tend to coincide with more amplified synoptic states associated with deeper, longer-lived cyclones (Hell et al., 2021; Lodise et al., 2022). In this context, upper-tropospheric forcing is a plausible discriminator: the polar-front
50 jet (and, secondarily, the subtropical jet) organizes and energizes midlatitude weather systems through jet-streak circulations and associated divergence aloft, thereby modulating surface cyclogenesis and intensity (Schultz et al., 2001; Bukenberger et al., 2025). A stronger and more zonally organized jet can enhance upper-level divergence and favour rapid deepening and persistence of extratropical cyclones—conditions that extend fetch and bolster swell generation (Bukenberger et al., 2025). Yet, despite these well-established dynamical links, the explicit connection between jet-stream variability and extreme coastal
55 swell remains only sparsely addressed in the wave-climate literature (Hell et al., 2021).

Motivated by this gap and using ERA5 reanalysis, we investigate the atmospheric circulation associated with extreme swell events in both hemispheres that affect the Peruvian coast, with particular emphasis on the dynamical characteristics of the jet stream. In addition, we assess the contribution of climate change to projected changes in the intensity of these events through an analogue-based framework.



60 2 Data and Methods

2.1 Extreme Swell Events Dataset

We define “extreme” swell events as those with anomalously high wave activity well beyond normal seasonal variability. For this study, anomalous swell events affecting the western coast of South America were identified using information provided by the Directorate of Hydrography and Navigation (DIHIDRONAV). These datasets include the number of special swell and
 65 wind warnings issued between 2008 and 2025, along with their respective intensities, start and end dates, as shown in Table 1.

Table 1: Extreme-swell events (2008–2025) based on special warnings issued by the DIHIDRONAV

Event	Year	Special Warning Number	Start date	End date	Maximum swell intensity	Direction
Southern Hemisphere						
E1	2011	31	19/06/2011	24/06/2011	Very strong	Southwest
E2	2014	28	01/07/2014	04/07/2014	Very strong	Southwest
E3	2017	61-62	11/08/2017	15/08/2017	Very strong	Southwest
E4	2017	68	07/09/2017	11/09/2017	Very strong	Southwest
E5	2023	26	27/05/2023	30/05/2023	Very strong	Southwest
Northern Hemisphere						
E6	2010	3-4	17/01/2010	21/01/2010	Strong	Northwest
E7	2010	09	17/02/2010	21/02/2010	Strong	Northwest
E8	2011	14-15	21/03/2011	29/03/2011	Strong	Northwest
E9	2012	5-6-7	06/02/2012	14/02/2012	Strong	Northwest
E10	2021	06	29/01/2021	02/02/2021	Strong	Northwest
E11	2025	02	10/01/2025	13/01/2025	Strong	Northwest

Note. According to the DIHIDRONAV classification, a “very strong” swell implies wave heights exceeding three times their normal conditions. In contrast, “strong” intensity indicates wave heights between two and three times the normal wave heights.

70 Five extreme swell episodes, classified as “very strong”, were identified along the Pacific coast of South America during the study period based on Peruvian Navy records (DIHIDRONAV, 2025). All occurred during austral winter months (May–September) and were associated with pronounced south-westerly swell directions originating in the South Pacific. We similarly identified a set of extreme swell events generating in the North Pacific in the past ~17 years. In total, we selected six benchmark events emanating from the NH (primarily boreal winter occurrences) classified as “strong” swells. The timing of each event’s peak swell at the coast was documented, and we analysed the atmospheric conditions in the days leading up to that peak.



75 To do this, we first estimated the travel time of swell from its source to the Peruvian coast using deep-water wave theory (Stewart, 2008). The group velocity of a swell packet is given by Eq. 1.

$$Cg = \frac{gT}{4\pi} \quad (1)$$

where g is gravitational acceleration (9.81 m s^{-2}) and T the wave period. The propagation time is given by Eq. 2

$$t = 4\pi X/gT \quad (2)$$

80 where X is the great-circle distance between the storm fetch and the coast. Using a representative distance of ~ 4035 km (between the main fetch region and southern Peruvian coast) and typical periods of 16–20 s (Tamayo, 2007), we obtained travel times of ~ 72 –90 hours (3–3.7 days) for the SH. For the NH, we obtained a distance of ~ 9200 km (related to the northern Peruvian coast) and travel times of ~ 192 –260 hours (8–11 days). These intervals were therefore used to analyse the atmospheric circulation leading up to each swell event.

85 **2.2 Synoptic composite analysis**

For each hemisphere's set of events, we performed a composite analysis of the atmospheric fields to identify common patterns. We used daily reanalysis data from 1991 to 2025 from ERA5 (Hersbach et al., 2020) in order to obtain daily maps for a window of 3–4 days (8–11 days for NH) prior to each event's swell arrival at the coast (based on swell travel time estimates).

90 These daily fields were averaged across events to compute composite anomalies of sea level pressure (SLP), geopotential height at 500 hPa and 250 hPa, 10-m and 250 hPa winds. We also analysed the significant height of wind waves (*SHWW*) over the open-ocean source regions to diagnose locally forced wind-sea generation. For each variable, anomalies were defined relative to the 1991–2020 day-of-year climatology and composited across event days. Statistical significance was assessed with a two-sided Mann–Whitney U test (Mann and Whitney, 1947).

2.3 Multiparametric jet diagnostics

95 To further characterize and understand the jet stream configuration in both hemispheres during these events, a multiparametric analysis of the jet stream was performed. For this, daily zonal wind data at 250 hPa from ERA5 were used, and the methodology developed by Collazo et al. (2024) was applied in order to have a better representation of upper-level jet features. In fact, this approach overcomes the limitations of traditional analysis based solely on jet latitude and intensity by incorporating additional metrics describing its dynamic structure, such as tilt, sharpness, meridional displacement (departure), number of branches, and
100 longitudinal extension. From the daily calculation of these diagnostic parameters, values were extracted and grouped accordingly. Boxplots were then produced to analyse the distributions and relationships among the different parameters, differentiating the signal associated with extreme events from the climatological behaviour.



2.4 Analogue's analysis

To assess the contribution of global warming to changes in 10-m wind speed, we applied the analogue method (e.g., Cattiaux et al., 2010; Yiou et al., 2017). This approach searches for events dynamically similar to the observed one and quantifies changes in intensity by comparing distributions derived from analogues of two periods with different levels of anthropogenic forcing. Because atmospheric circulation is held fixed, the resulting differences highlight the thermodynamic influence of climate change.

The analogue analysis is based on ERA5 data for 1950–2025. Flow analogues were identified by selecting days with similar SLP, Z500, and Z250 fields, using the mean standardized Euclidean distance to ensure equal weighting among variables (Barriopedro et al., 2025). For each event, the expected wind speed was reconstructed by randomly sampling one of the N best analogues within the $[-L, L]$ -day window surrounding the corresponding calendar date. A sensitivity analysis performed for $N = \{20, 35, 50\}$ and $L = \{31, 45, 61\}$, as well as for different analogue-search domains, showed no relevant changes in the results. Based on these reconstructed wind speeds, differences in median values between the past (1950–1987) and present (1988–2025) periods were then assessed for statistical significance using the Mann–Whitney U test (Mann and Whitney, 1947). After identifying flow analogues, we examined the role of climate variability modes by extracting the monthly Southern Annular Mode (SAM) index for SH events and the Pacific Decadal Oscillation (PDO) index for NH events on the analogue dates. The SAM represents the leading mode of extratropical Southern Hemisphere variability and reflects latitudinal shifts in the westerly wind belt encircling Antarctica, with positive (negative) phases associated with stronger, poleward-shifted (weaker, equatorward-shifted) westerlies and corresponding changes in storm-track position and intensity (Fogt and Marshall, 2020). The SAM index was computed from monthly ERA5 SLP between 40°S and 65°S following Marshall (2003). The PDO is a major mode of decadal variability in the North Pacific, marked by basin-wide SST anomalies and associated wind-stress changes. Its positive phase leads to an eastward extension and poleward displacement of the North Pacific jet stream, along with increased mid-latitude cyclonic activity (Wills et al., 2019). The PDO index was obtained from NOAA (https://www.ncei.noaa.gov/access/monitoring/pdo/accessed, November 2025).

3 Results

The study first examines events originating in the SH and subsequently those in the NH, allowing for a comparative assessment of their large-scale atmospheric drivers. For each hemisphere, the analysis begins with a synoptic characterization to establish the dynamical processes responsible for event development. Building on this, we then deepen the investigation by focusing on the specific configuration and role of the upper-level jet stream, a key driver of extreme weather patterns (e.g., Xu et al., 2023; García-Burgos et al., 2023; Collazo et al., 2024). Finally, to contextualize our findings within a broader climatological framework, we search for analogues of the previously described atmospheric circulation patterns in order to evaluate possible changes in event intensity over time. This progression, from synoptic overview to jet-stream diagnostics and flow-analogue assessment, provides a coherent framework to investigate both the physical mechanisms and temporal changes of the events.

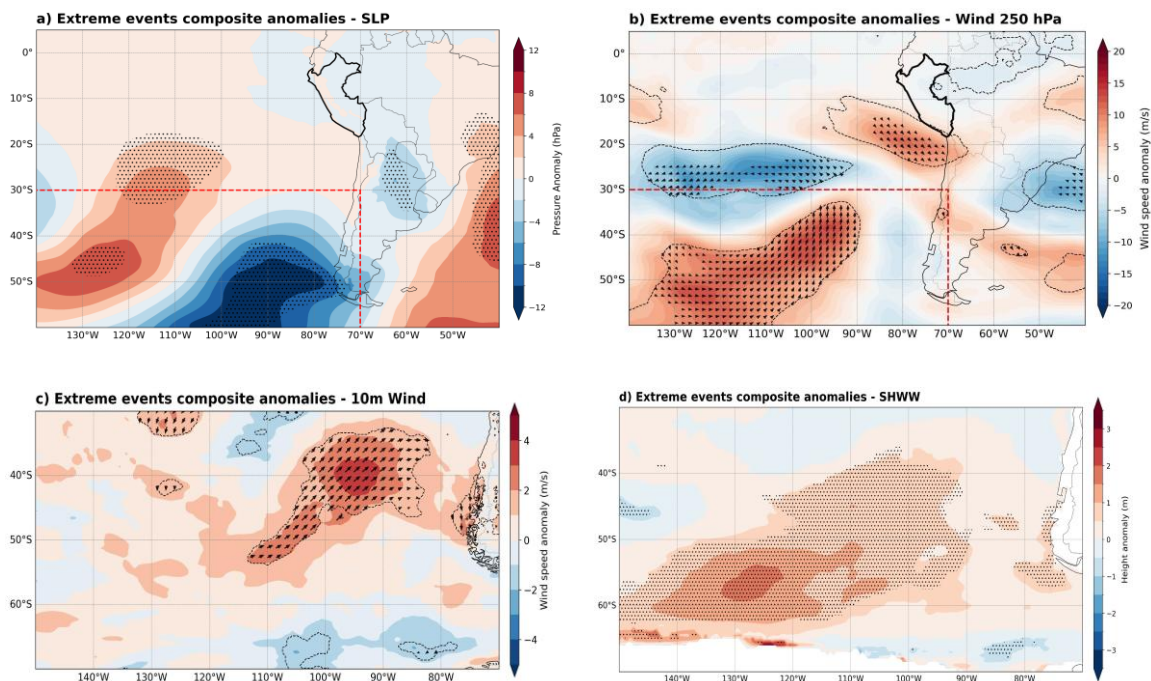


135 3.1 Southern Hemisphere Extreme Swell Events

3.1.1 Synoptic Patterns

The composite fields for SH events E1–E5, averaged over days D–4 to D–3 relative to D0, reveal a well-organized barotropic disturbance over the southeast Pacific (Fig. 1a and Fig. S1). SLP exhibits a pronounced negative anomaly south of 40°S and between about 120°–70°W, flanked by positive SLP anomalies to the southwest and southeast of the low (Fig. 1a). This tripolar structure reflects a deep extratropical cyclone embedded between broad anticyclonic anomalies on both sides of the basin. The resulting meridional pressure gradient is strongly enhanced along the northern and north-eastern flank of the low over the mid-latitude Pacific. The vertical coherence of this disturbance is evidenced by the close alignment of the SLP, Z500, and Z250 anomaly centres (Fig. S1 - Supporting Information), which supports the interpretation of a mature, vertically coherent barotropic disturbance.

145



150 **Figure 1: Southern Hemisphere composite anomalies during extreme-swell events (E1–E5; MJJAS).** Panels (a)–(b) show large-scale conditions over 140°W–40°W and 5°N–60°S: (a) sea-level pressure (SLP) anomaly (shading) and (b) 250-hPa wind-speed anomaly (shading) with wind-anomaly vectors. The red boxes in (a) and (b) indicate the regional domain analyzed in (c) and (d) (150°W–70°W, 30°–70°S): (c) 10-m wind-speed anomaly (shading) with wind-anomaly vectors and (d) significant height of wind waves (SHWW) anomaly (shading). Anomalies are computed relative to the 1991–2020 MJJAS climatology and averaged over days D–4 to D–3 relative to day D0. Statistical significance at $p < 0.05$ (two-sided Mann–Whitney U test) is indicated by stippling in (a) and (d), and by dashed contours enclosing the wind vectors in (b) and (c). The Peruvian coastline is outlined to indicate the impacted coastal sector.



At upper levels, the 250-hPa wind composite (Fig. 1b) exhibits an elongated band of enhanced winds relative to the
155 climatology, between about 30°–60°S and 130°–90°W, broadly collocated with the surface pressure tri-pole and the 10-m
wind maximum. The jet core follows a relatively straight southwest–northeast trajectory as it approaches South America.

The near-surface wind response at 10-m (Fig. 1c) is consistent with this pressure pattern. A wide corridor of positive wind-
speed anomalies spans roughly 35°–55°S, with vectors indicating intensified westerly to south-westerly flow over the central
southeast Pacific. Within this corridor, the strongest anomalies are found between about 100°–90°W, oriented along a
160 southwest–northeast axis that points toward the Peruvian and Chilean coasts. On the equatorward side of the cyclone, the
anomalous flow curves from westerly to north-westerly as it approaches South America, effectively lengthening the fetch over
which the enhanced winds act on the ocean surface. Weaker or negative wind-speed anomalies to the north and south of this
band delineate the core of the storm-track intensification associated with the extreme events.

The impact of this strengthened fetch on local wave generation is captured by the SHWW composites (Fig. 1d). Positive
165 SHWW anomalies exceeding 1 m organize into a broad, zonally elongated swath between about 38°–65°S and 150°–89°W,
broadly collocated with—and slightly poleward of—the 10-m wind-speed anomalies. This partial offset is expected, because
wind-wave growth integrates wind forcing over the evolving fetch and depends on the absolute wind field rather than anomalies
alone. Negative or near-zero anomalies to the north indicate that the subtropical wave field remains relatively unperturbed,
highlighting the key role of this high-latitude belt as the primary open-ocean source of the extreme swells that reach the
170 Peruvian coast a few days later.

3.1.2 Southern Jet Stream Characteristics

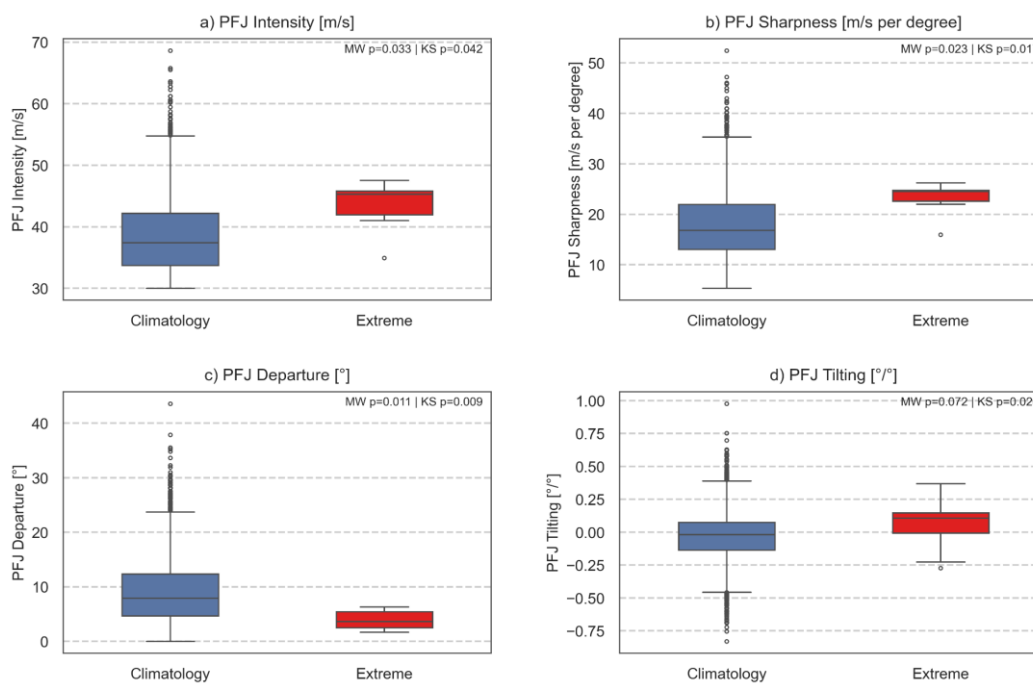
Having characterized the synoptic structure of the SH events, we next examine the associated upper-level circulation, focusing
in particular on the austral wintertime polar-front jet (PFJ) over the Southeast Pacific. To quantify changes in the PFJ during
extreme-swell events, we construct boxplots for several jet parameters, comparing their climatological distributions with those
175 observed during the events. The PFJ exhibits marked differences between extreme-swell cases and the seasonal climatology
(Fig. 2). PFJ intensity (Fig. 2a) shows a clear shift toward higher values during E1–E5: event-day medians lie several m s^{-1}
above the climatological median, and the interquartile range is substantially narrower. According to the summary statistics in
Supplementary Figure S3, both the Mann–Whitney and Kolmogorov–Smirnov tests indicate that this enhancement in PFJ
strength is statistically significant ($p < 0.05$).

180 PFJ sharpness, a metric that quantifies how narrowly the jet core is confined latitudinally, also increases during extreme events
(Fig. 2b). The distribution for event days is concentrated around larger meridional wind-speed gradients, with very little overlap
with the climatological upper quartile. Physically, this indicates that the jet is not merely stronger but also exhibits a steeper
gradient between its core and the surrounding flow when extreme swell develops.

Differences in jet orientation are captured by the departure and tilting metrics, which respectively describe the meridional
185 coherence and inclination of the jet. Departure measures the spread of the latitudinal positions of the wind maxima along the
jet axis and tilting, in contrast, quantifies the zonal inclination of the jet by evaluating the slope of a linear regression fitted to



190 the tracked latitudes of the jet core (Barriopedro et al., 2023). PFJ departure displays markedly smaller values for E1–E5, with event-day boxes clustered near low departures while climatological values span a wide range, including numerous large outliers (Fig. 2c). This indicates that during extreme-swell events, the PFJ maintains a compact, well-organized structure, with a single core of maximum winds. PFJ tilting exhibits a modest but significant shift toward more positive values for extremes, implying a slightly more consistent southwest–northeast orientation of the jet as it crosses the South Pacific (Fig. 2d).



195 **Figure 2: Southern Hemisphere jet diagnostics during extreme-swell events E1–E5 (MJJAS). Boxplots of polar-front jet (PFJ) significant metrics for event days (red) versus austral winter climatology (blue) from ERA5 250-hPa winds: (a) PFJ intensity, (b) PFJ sharpness, (c) PFJ departure and (d) PFJ tilting. P-values from Mann–Whitney and Kolmogorov–Smirnov tests are shown above panels.**

As summarized in Table S1 from Supporting Information, tilting differences reach statistical significance in at least one of the tests, whereas other positional parameters (e.g., jet latitude or longitudinal extent) do not. Overall, the SH composites show that extreme swell is preceded by a PFJ that is stronger, sharper, less latitudinally variable, and weakly positively tilted compared with the broader austral winter population. While these analyses characterize the large-scale circulation associated with extreme swell events, they do not address how such configurations may be evolving over time. To explore this aspect, we next adopt a flow-analogue approach.

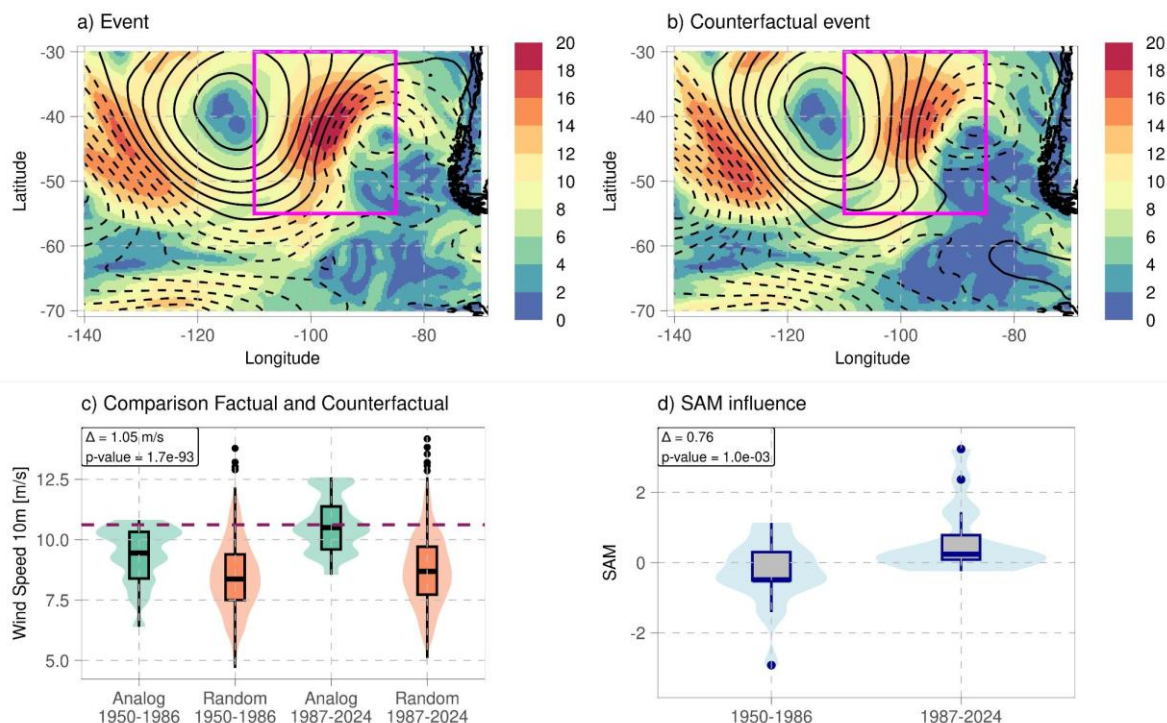
200



3.1.3 Analogues Analysis

Records of extreme wave events span only a few years, so to assess how climate change might be altering their characteristics, we rely on flow analogues. Figure 3 illustrates the results of applying this method to event E1, with similar patterns found for the other SH events. The wind speed at 10-m and the SLP of the event according to the ERA5 reanalysis are shown in Fig. 3a. As previously analysed, a strong pressure gradient is identified between an anticyclone and a cyclone in the South Pacific, resulting in intense surface winds with a considerable meridional component. By removing the climate-induced shift, quantified as the difference in medians between the present and past flow analogues, E1 yields weaker surface winds due to a lower pressure gradient (Fig. 3b). A more comprehensive comparison between the reconstruction of wind speed at 10-m in the region indicated in panels a and b is shown in Fig. 3c. Days with random atmospheric circulation show greater variability in wind intensity than days with flow analogues; however, the latter tend to have stronger winds (see the medians in the boxplots). Regarding the comparison between analogue flows in the past and present periods, there has been a significant increase in wind speed in recent decades, meaning that similar atmospheric circulation in the present climate results in stronger winds in the South Pacific.

Because the SAM is the dominant mode of climate variability in the extratropical SH (Fogt and Marshall, 2020), we also examine its role in shaping this event (Fig. 3d). The monthly SAM index associated with past and present flow analogues indicates a significant difference, with recent analogues predominantly associated with positive values of the index. A positive phase of the SAM strengthens and shifts the belt of SH westerly winds poleward, increasing windiness over the high latitude while weakening westerlies in many midlatitude regions. Consequently, positive SAM conditions are associated with stronger winds across the southern half of the study region (Fig. S2 - Supporting Information), reinforcing the intensification already suggested by the analogue-based wind reconstructions. This relationship helps explain the differences between the observed event and its counterfactual. In the counterfactual reconstruction (Fig. 3b), winds are weaker over the southern portion of the domain compared with the observed event (Fig. 3a). This weakening is consistent with a shift toward less positive SAM conditions in the past analogue period, indicating that part of the observed wind amplification can be attributed to the recent tendency toward more positive SAM phases. Previous studies have shown that this positive SAM trend is largely driven by stratospheric ozone depletion and increasing greenhouse gas concentrations (Abram et al., 2014; Fogt and Marshall, 2020; King et al., 2023; Purich et al., 2025). These external forcings enhance the likelihood of positive SAM states, thereby creating background conditions that favor stronger winds in the high-latitude South Pacific. All SH events examined here exhibit this SAM-related wind intensification, with the sole exception of E3 which does not show a significant influence of this climate mode.



235 **Figure 3: Analogue analysis for the E1 event. (a) Wind speed at 10-m (shaded) and SLP (contours) observed during E1 in the**
ERA5 reanalysis. Dashed contours indicate pressures below 1013 hPa. (b) Counterfactual reconstruction of 10-m winds (shading)
and SLP (contours), obtained by removing the climate-change signal—defined as the median differences between present and past
analogue flows—from the observed event. (c) Mean wind speed at 10m over the box, indicated in panels (a) and (b), reconstructed
from flow analogues (green) and random (orange) days of the past (1950-1986) and present (1987-2024) period. The dotted
horizontal line indicates the intensity of the event observed in ERA5. The legend shows the difference in medians between the
 240 **present and past periods for wind speed at 10-m for days with similar flow and its statistical significance according to the Mann-**
Whitney U test. (d) Monthly SAM associated with days with flow analogues for the past and present periods. The difference
between medians for both periods and statistical significance is indicated in the legend.

3.2 Northern Hemisphere Extreme Swell Events

245 3.2.1 Synoptic Patterns

The composite fields for NH events E6–E11, averaged over days D–11 to D–8 prior to D0, show a large-scale, vertically coherent disturbance over the North Pacific (Fig. 4). SLP exhibits a deep negative anomaly centred near 30–40° N in the central–western basin. Positive SLP anomalies are weaker and more localized, occurring mainly over the north-eastern Pacific–North American/Arctic sector, with no coherent anticyclonic ridge elsewhere. Thus, in this case, the preconditioning atmospheric pattern is characterized by a single basin-scale deep low with comparatively modest surrounding highs (Fig. 4a).

250

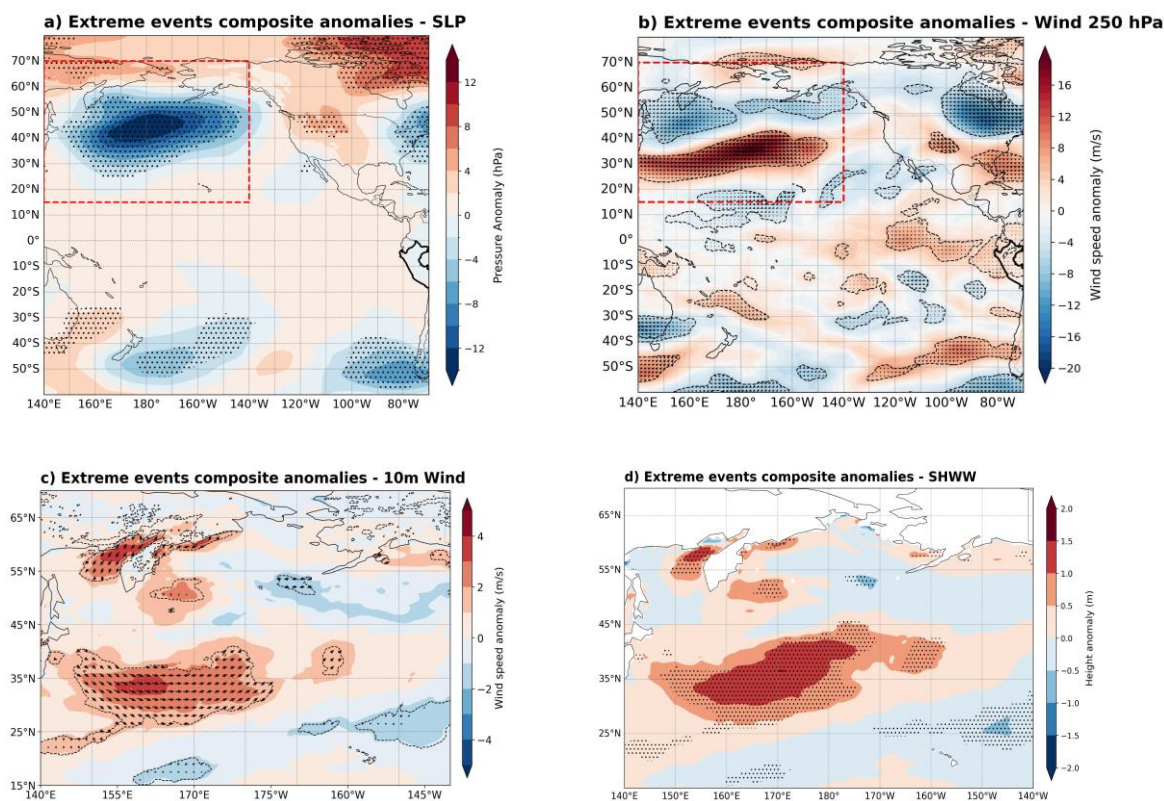


This configuration tightens the meridional pressure gradient along the southern flank of the low, favouring an enhanced belt of westerly to north-westerly flow across the midlatitude North Pacific.

The barotropic nature of this storm configuration is evidenced by the consistency among SLP, 500-hPa, and 250-hPa geopotential height anomalies (Fig. S3 - Supporting Information). Negative height anomalies at Z500 and Z250 are nearly vertically aligned with the SLP minimum over the central–western North Pacific, and positive anomalies arch over the subpolar and continental sectors at all three levels.

255 vertically aligned with the SLP minimum over the central–western North Pacific, and positive anomalies arch over the subpolar and continental sectors at all three levels. This three-level coherence—from the surface pressure field through the mid-troposphere to the upper-tropospheric flow—confirms that the storm complex associated with events E6–E11 is embedded within a vertically stacked, slowly evolving barotropic structure. In this configuration, the cyclone sustains enhanced W–NW low-level winds over a broad midlatitude sector.

260



265

Figure 4: Northern Hemisphere composite anomalies during extreme-swell events (E6–E11; DJFM). Panels (a)–(b) show basin-scale anomalies over 140°E–70°W and 80°N–60°S, averaged over days D–11 to D–3 relative to day D0: (a) sea-level pressure (SLP) anomaly (shading) and (b) 250-hPa wind-speed anomaly (shading) with wind-anomaly vectors. Panels (c)–(d) show a zoomed view of the North Pacific swell-source region (140°E–140°W, 15°–70°N): (c) 10-m wind-speed anomaly (shading) with wind-anomaly vectors and (d) significant height of wind waves (SHWW) anomaly (shading). Anomalies are computed relative to the 1991–2020 DJFM climatology. Statistical significance at $p < 0.05$ (two-sided Mann–Whitney U test) is indicated by stippling in (a) and (d), and by dashed contours enclosing the wind vectors in (b) and (c). The Peru outline is highlighted for reference.



270 Aloft, the 250-hPa wind-speed anomalies reveal a strongly intensified North Pacific jet, with a well-defined core between
about 30° and 40° N that is significantly stronger than the seasonal climatology (Fig. 4b). The anomalous jet is oriented from
west-southwest to east-northeast across the central basin, closely collocated with the surface cyclone. This upper-level
enhancement indicates that the extreme-swell events occur when the midlatitude jet stream locally accelerates and becomes
more zonally extended over the North Pacific, providing sustained upper-tropospheric support for the surface cyclone and
reinforcing the low-level pressure gradients along its southern flank. Consistent with this large-scale pressure and upper-level
275 jet configuration, the near-surface wind response strengthens over the North Pacific source region. The 10-m wind-speed
anomaly composite displays a wide swath of positive anomalies between about 25° and 40° N, extending from roughly 145°
E to 175° W (Fig. 4c). Within this band, wind speeds exceed the climatological mean, with the strongest and most coherent
anomalies concentrated on the southern side of the cyclonic system where the pressure gradient is strongest. The vectors reveal
a predominantly W–NW orientation, which sets up a long and relatively straight fetch directed toward the subtropical eastern
280 Pacific. To the south and north of this corridor, weak or negative anomalies indicate that the anomalous momentum input is
strongly focused within a narrow mid-latitude belt rather than spread across the whole basin.

The impact of this persistent wind forcing on the sea state is captured by the SHWW composite (Fig. 4d). A broad, statistically
significant band of positive SHWW anomalies spans the open-ocean source region between about 27° and 45° N, overlapping
and extending downstream of the 10-m wind-speed maximum. In the NH, wind and SHWW anomalies are more tightly co-
285 located, consistent with a narrower, more geographically confined wind-forcing corridor over the North Pacific source region.
This pattern indicates an unusually energetic wind-sea that has grown under sustained W–NW winds over several days.
Negative or near-zero SHWW anomalies equatorward of ~25° N, including around Hawaii, indicate little enhancement (and
locally slight suppression) of wind-sea relative to DJFM climatology in the subtropical central Pacific. Given that the
composite window is 8–11 days before coastal impact, these fields capture the stage when the local wind-sea is still being
290 generated in the central basin while the resulting swell has already begun its long-range propagation toward South America.

3.2.2 Northern Jet Stream Characteristics

The multi-parametric description of the jets for the NH events, E6–E1, shows statistically robust differences emerge in both
the subtropical jet (STJ) and the PFJ relative to the boreal winter climatology (Fig. 5).
295 STJ diagnostics reveal a systematic strengthening and structural tightening of the upper-level flow during extreme-swell cases
(Fig. 5a–f). STJ sharpness (Fig. 5a) is clearly larger for event days, with the red boxes shifted upward and a reduced
interquartile range compared with the climatology. The maximum intensity of the western branch (Fig. 5b) and the zonal-mean
STJ intensity (Fig. 5c) are likewise enhanced, while the eastern-branch intensity (Fig. 5e) also shifts toward higher values. The
western branch extends over a longer longitude range on event days (Fig. 5d), and its tilting (Fig. 5f) exhibits more positive
300 values, indicating a more coherent southwest–northeast tilt of the western branch, consistent with the WSW–ENE jet axis in

Figure 4b. Table S2 from Supporting Information, confirms that these changes in sharpness, intensity, extent, and tilting are all significant at $p < 0.05$ in at least one of the non-parametric tests.

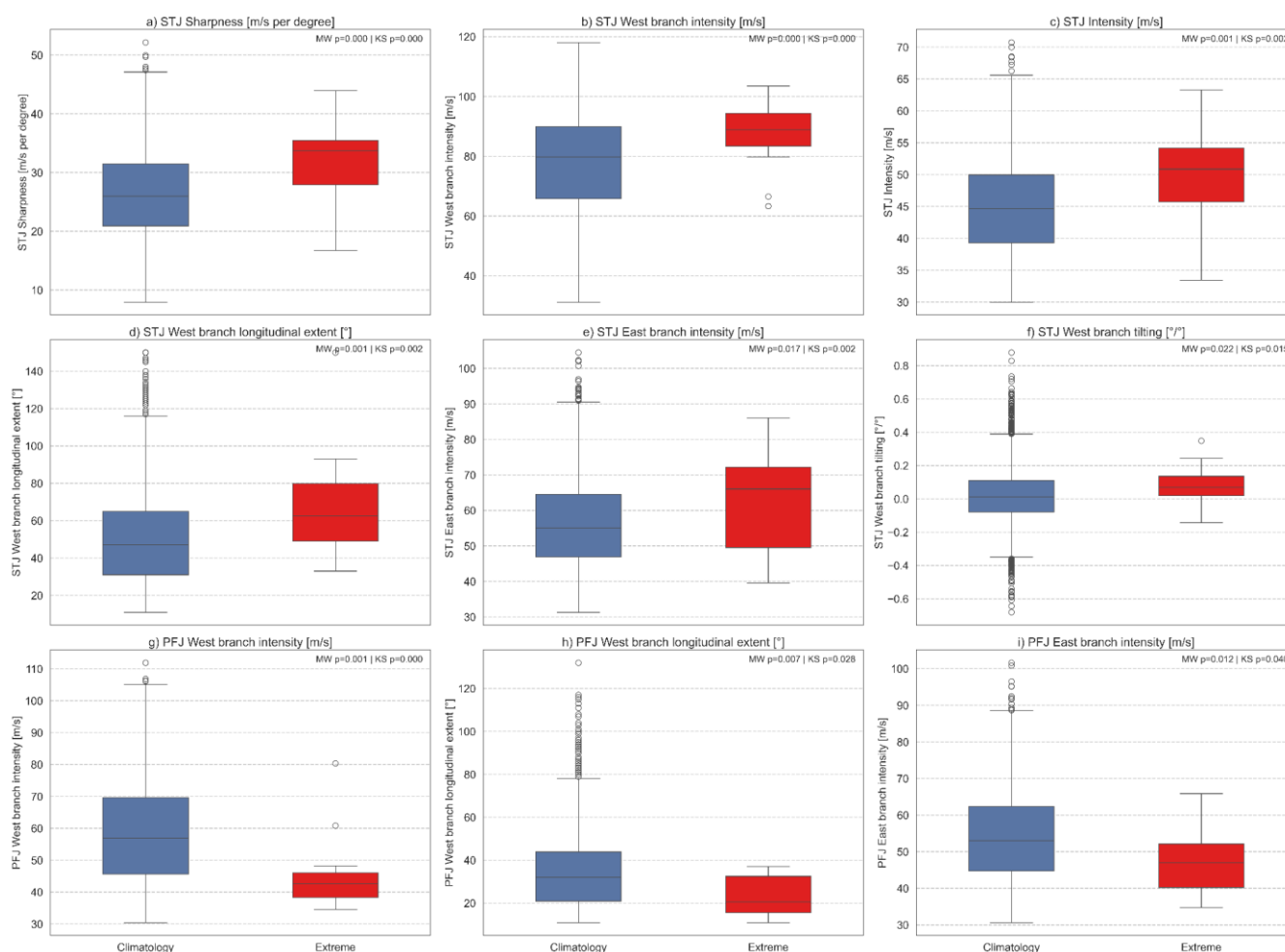


Figure 5: Northern Hemisphere jet diagnostics during extreme-swell events E6–E11 (DJFM). Boxplots of the statistically significant subtropical-jet (STJ) and polar-front-jet (PFJ) metrics derived from ERA5 250-hPa winds. (a) STJ sharpness, (b) STJ west-branch intensity, (c) zonal-mean STJ intensity, (d) STJ west-branch longitudinal extent, (e) STJ east-branch intensity, (f) STJ west-branch tilting, (g) PFJ west-branch intensity, (h) PFJ west-branch longitudinal extent, and (i) PFJ east-branch intensity. Event-day distributions (red) are contrasted with the seasonal climatology (blue); Mann–Whitney and Kolmogorov–Smirnov p -values are shown above each panel. A summary of the statistically significant parameters is provided in Supplementary Figure S3.

310 PFJ metrics (Fig. 5g–i) show the opposite behavior. West-branch PFJ intensity (Fig. 5g) is significantly weaker during E6–E11 than in the climatology, with lower medians and a narrower spread. The longitudinal extent of the western branch (Fig. 5h) is also reduced, indicating fewer cases with a long, continuous PFJ across the basin. East-branch PFJ intensity (Fig. 5i)

tends to be lower for event days as well. As summarized in Table S3 (Supporting Information), these PFJ differences are statistically significant for both tests, highlighting that NH extreme swell co-occurs with a markedly intensified and more organized STJ together with a weaker, less extensive PFJ.

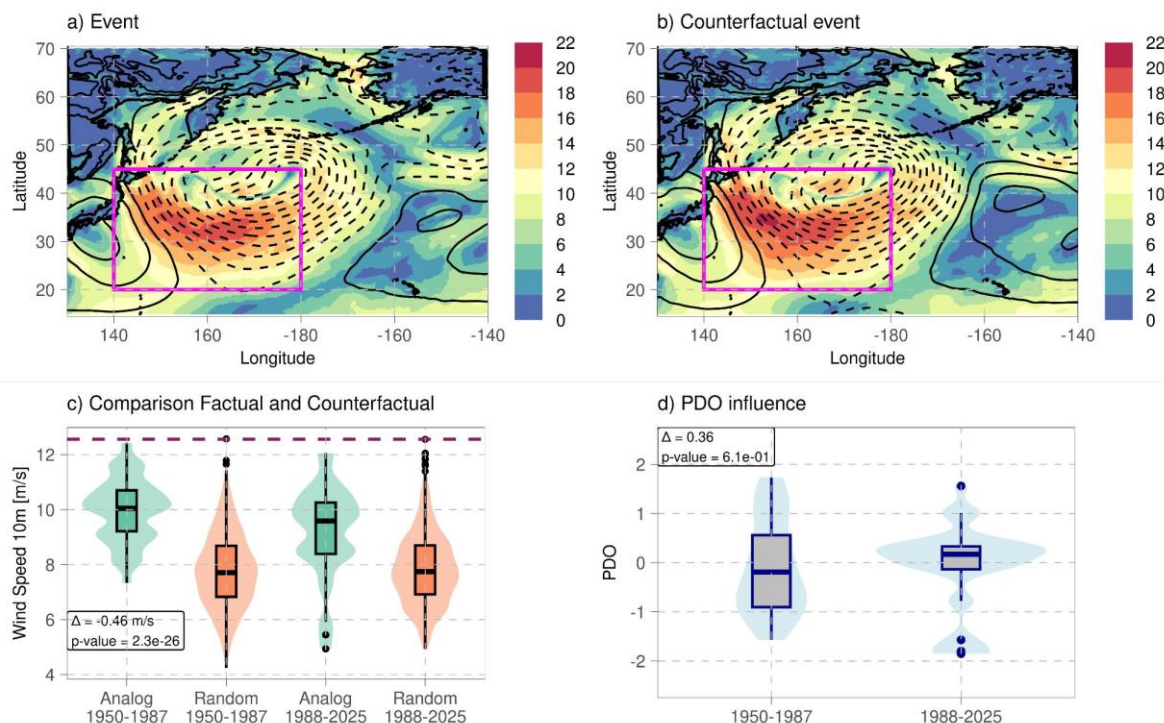
3.2.3 Analogues Analysis

For NH events, the analogue-based analysis highlights notable differences between the three most recent events (E9–E11) and the three preceding ones (E6–E8). To illustrate the latter group, event E7 is shown in Fig. 6. This event is characterized by a very deep cyclone over the north-western Pacific and anticyclonic conditions over Japan, with the strongest winds exhibiting a northwest–southeast orientation within the subtropical belt (Fig. 6a). After removing the climate-induced shift, we find that the event would have been more intense under counterfactual conditions—i.e., with reduced anthropogenic influence on the climate (Fig. 6b). This behaviour is also evident in the boxplots of the flow analogues: the analogues for the past period exhibit a significantly higher median wind speed compared with those for the present (Fig. 6c). For both periods, however, analogue days generally show stronger winds than days selected under random circulation. Furthermore, the natural variability associated with the PDO does not contribute to explaining the differences between past and present analogues (Fig. 6d).

In contrast, the three most recent NH events exhibit an increase in wind speed. To examine this behavior in greater detail, event E9 is presented in Fig. 7. This event was characterized by an intense surface cyclone situated in mid-latitudes over the North Pacific (Fig. 7a), which, under counterfactual conditions, would have been less intense (Fig. 7b). Boxplots of the analogue flows further highlight this significant increase in wind intensity during the present period (Fig. 7c). It is important to note that this increase is observed only under constrained circulation; wind speeds under random circulation remain essentially unchanged between the two periods.

For both E9 and E11, we find a significant contribution from the PDO, since flow analogues from the present period tend to occur more frequently under the negative phase of the PDO (Fig. 7d). However, this phase exerts an influence on surface wind speed that is opposite to that detected with the analogues, as it contributes to a slowdown in wind speed (Fig. S4 - Supporting Information). This discrepancy indicates that additional factors must contribute to the observed wind speed increases in the flow analogues for the recent period, as well as the differences found between the different events.

The western North Pacific, at subtropical and mid-latitudes, is characterized by high interannual and decadal variability, with multiple interacting factors modulating atmospheric and oceanic circulation (Henley, 2017). This intrinsic variability underlies the IPCC's low confidence in attributing the observed changes in extratropical cyclones over the North Pacific to anthropogenic climate change (Seneviratne et al., 2021).



345 **Figure 6. Analogue analysis for the E7 event. (a) Wind speed at 10-m (shaded) and SLP (contours) observed during E7 in the ERA5 reanalysis. Dashed contours indicate pressures below 1013 hPa. (b) Counterfactual reconstruction of 10-m winds (shading) and SLP (contours), obtained by removing the climate-change signal—defined as the median differences between present and past analogue flows—from the observed event. (c) Mean wind speed at 10m over the box, indicated in panels (a) and (b), reconstructed from flow analogues (green) and random (orange) days of the past (1950-1987) and present (1988-2025) period. The dotted horizontal line indicates the intensity of the event observed in ERA5. The box shows the difference in medians between the present and past periods for wind speed at 10-m for days with similar flow and its statistical significance according to the Mann-Whitney U test. (d) Monthly PDO associated with days with flow analogues for the past and present periods. The difference between medians for both periods and statistical significance is indicated in the box.**

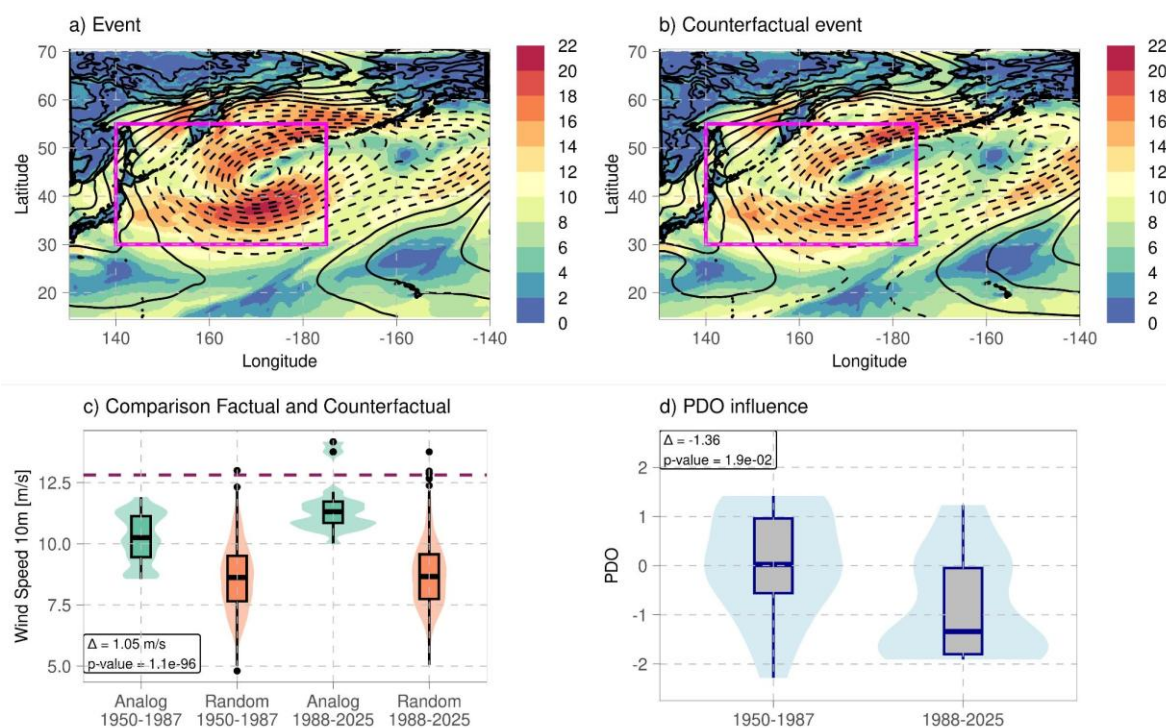
350

4 Discussion

355 Extreme swell events affecting the Peruvian coast arise from two seasonally distinct storm tracks, the synoptic pressure pattern and the jet component that intensifies differ markedly between hemispheres, and these differences help explain the contrast in coastal swell class.

In the Southern Hemisphere, preconditioning typically resembles a cyclone–anticyclone couplet: a deep subpolar low is accompanied by a robust subtropical high, yielding a tight meridional pressure gradient along the storm’s equatorward flank. This configuration supports a broad, persistent belt of south-westerly surface winds over the south-eastern Pacific, favouring
 360 efficient wind–wave growth over a long open-ocean fetch. Consistent with our jet diagnostics, SH events co-occur with a

stronger and sharper PFJ that is generally less meandering than the winter climatology, reinforcing the storm–jet coupling required to sustain these wind corridors and allowing some events to reach the ‘very strong’ swell class at the Peruvian coast.



365

Figure 7. Same as figure 6 for the E9 event.

In the Northern Hemisphere, the surface pattern is instead dominated by a deep central–western North Pacific low, while surrounding positive SLP anomalies are comparatively weak and spatially localized, so a clear cyclone–anticyclone tri-pole is not a defining feature. Upper-level support also shifts: NH events are characterized by a marked intensification and zonal extension of the STJ, whereas the PFJ weakens and becomes less continuous. The resulting surface winds are typically westerly to north-westerly along the equatorward flank of the low and can still transmit swell energy toward Peru, but the longer propagation distance and the need to cross the equator favour greater attenuation and dispersion, consistent with NH events reaching at most the ‘strong’ class in our sample.

Overall, the results show a significant hemispheric asymmetry that is crucial for interpreting how remote storms project wind forcing into the ocean and for translating upper-level diagnostics into early identification of swell-generating situations

375



Beyond the synoptic similarities and contrasts described above, it is also crucial to explore how external forcings—particularly anthropogenic climate change—may influence the occurrence and intensity of these swell-generating configurations. In this regard, the influence of climate change appears to be more pronounced and consistent among events originating in the SH than in the NH. Across all SH events, atmospheric circulations analogous to those observed are associated with stronger 10-m winds
380 in the recent period, reflecting the increased prevalence of the positive SAM phase. Collectively, these results indicate that climate change exerts a discernible and coherent influence on SH extratropical wind patterns, underscoring the region's sensitivity to both anthropogenic forcing and internal climate variability.

To further elucidate the role of other climate modes influencing the South Pacific, we also examined changes in the predominant phases of the El Niño-Southern Oscillation (ENSO) associated with the flow analogue days between the past and
385 present periods. In the austral winter, ENSO modulation over the region is quite weak due to a predominance of the neutral phase (Cai et al. 2021). A significant signal is observed only in events E3 and E4, where past-period analogues are more frequently associated with La Niña conditions, whereas in the present period, neutral and, in some cases, El Niño phases predominate (Fig. S5 - Supporting Information). This shift corresponds to an intensification of winds in subtropical latitudes and a reduction in mid-latitudes (Fig. S6 - Supporting Information), opposing the positive SAM signal. In contrast, the PDO
390 shows no significant association with wind speed in the South Pacific, so the frequency of analogues under the different phases is not analysed.

In contrast to the SH, the attribution of changes in surface circulation during flow-analogue events in the NH remains less straightforward, given that some events have intensified in recent decades whereas others have weakened. The increased occurrence of analogues associated with the negative phase of the PDO in the recent period for events E9 and E11 introduces
395 additional ambiguity, since the influence of the PDO appears to oppose the circulation changes inferred from the analogues. To further elucidate these relationships, the effects of additional modes of internal variability in the North Pacific were examined (Table S4 - Supporting Information).

The influence of ENSO on these events appears limited, with only E8 exhibiting a significant change in index values between periods. In the recent period, analogues for this event tend to occur predominantly during El Niño phases, which are associated
400 with stronger winds over the western North Pacific (Table S4 - Supporting Information). ENSO also serves as the primary driver of the Pacific–North American (PNA) pattern, a leading mode of low-frequency variability in the NH extratropics, particularly during boreal winter (Wang and Yang, 2023). Nevertheless, only the flow analogues of E11 exhibit modulation consistent with the PNA.

The Arctic Oscillation (AO), especially in its positive phase, modifies large-scale pressure gradients and induces changes in
405 wind anomalies over the North Pacific during winter. Positive AO phases correspond to weaker winds mainly in January, over subtropical latitudes and along the Asian coast, which may have contributed to the wind intensity changes observed in the analogous circulations of events E6 and E7 (Table S4 - Supporting Information). Another mode that exerts its influence on various events is the Western Pacific (WP) pattern. The WP is a primary mode of low-frequency variability over the North Pacific (Barnston and Livezey, 1987; Wallace and Gutzler, 1981). During winter and spring, the pattern features a north–south



410 dipole of anomalies, with one centre over the Kamchatka Peninsula and a broad, oppositely signed centre spanning parts of south-eastern Asia and the western subtropical North Pacific (Ma and Zhang, 2018). Consequently, a strong positive phase of this pattern corresponds to intense winds in the mid-latitudes and weak winds in the subtropics. Therefore, the higher frequency of analogues under the positive phase of the WP in the present period is associated with changes in wind intensity that varies within the target region considered for the reconstruction of the analogues (Table S4 - Supporting Information).

415 Finally, the Interdecadal Pacific Oscillation (IPO), a basin-wide counterpart of the PDO (Dong and Dai, 2015), exerts comparable influences on wind variability in the western North Pacific that closely mirrors the PDO-related signal. Its negative phase is associated with reduced wind speeds across the region, which is consistent with the changes recorded in events E6 and E8.

The analysis of internal variability and its contribution to the changes detected by the analogues does not reveal a dominant mode capable of explaining the reported patterns. This suggests the involvement of additional factors. Several reanalyses indicate that the observed weakening of surface winds in this sector of the Pacific Ocean is largely influenced by variations in aerosol concentrations (Deng et al., 2021). In addition, anomalous changes in Arctic Sea ice during the preceding summer and autumn have been shown to strongly modulate the variability of winter extratropical cyclones over the North Pacific (Chen and Sun, 2023). Finally, the pronounced northward displacement and intensification of midlatitude storm-track activity during boreal winters in the North Pacific since the early 1980s have been attributed to subtropical tropospheric warming. This warming enhances the meridional temperature gradient in midlatitudes, counteracting the opposing influence of Arctic warming, which tends to reduce near-surface temperature gradients and suppress storm-track activity (Hsu et al., 2025). These external forcings, however, are not explicitly analysed in this study, and further research would be required to determine their direct influence on the analogues.

430 In summary, the results presented here align with the conclusions of the IPCC AR6 report, which notes low confidence in attributing observed changes in cyclone intensity over the North Pacific to anthropogenic climate change, primarily due to substantial interannual and decadal variability (Seneviratne et al., 2021). Conversely, there is high confidence that changes in the SH can be partly attributed to anthropogenic forcing.

5 Conclusions

435 We examined how extreme swell events affecting the Peruvian coast are preconditioned by large-scale atmospheric circulation in both hemispheres, with particular emphasis on the dynamical configuration of the upper-tropospheric jets and their coupling with barotropic storm systems. Using ERA5 reanalysis, a multiparametric jet diagnostic, and a flow-analogue framework, we contrasted Southern and Northern Hemisphere events to assess both the dynamical pathways leading to extreme swell and the imprint of recent climate change on the associated near-surface winds.

440 The main conclusions are:



- Extreme swell events in both hemispheres are preceded by a vertically coherent cyclone–jet configuration (surface to ≥ 250 hPa). In the NH, preconditioning is dominated by a very deep North Pacific low, whereas in the SH it more often reflects a tripolar pattern that tightens the pressure gradient and sustains the wind corridor that projects swell energy toward Peru.
- 445 • In the SH, extreme swell episodes co-occur with a PFJ that is stronger, sharper, generally with positive tilting, and less meandering than the winter climatology. The jet core remains closer to its preferred latitude, and its modest southwest–northeast tilt contributes to focusing persistent southwesterly winds over the southeast Pacific, creating the primary swell-generating fetch for Peru.
- In the NH, extreme swell events arise under a distinct jet configuration: the STJ intensifies, sharpens, and extends
450 longitudinally, while the PFJ becomes weaker and less continuous. This redistribution of upper-level momentum favors deep barotropic cyclones over the central–western North Pacific and sustains a narrow belt of anomalously strong westerly to northwesterly winds that can still transmit swell energy across the equator to northern Peru.
- Flow-analogue reconstructions indicate that climate change has strengthened surface winds during extreme-wave events originated in the SH by enhancing the synoptic pressure gradients that generate them. This intensification is
455 partially amplified by the recent trend toward more positive SAM phases—driven largely by ozone depletion and greenhouse-gas forcing—which favors stronger westerlies across the high-latitude South Pacific, a pattern consistently found across all SH events except E3.
- For NH events, analogue-based reconstructions reveal no consistent climate-change signal: while some recent events (E9–E11) exhibit stronger winds, others (E6–E8) weaken under present-day conditions. However, these contrasts
460 cannot be explained by a single mode of internal variability; neither the PDO, ENSO, PNA, AO, WP nor IPO accounts for the observed differences. This highlights that the high interannual and decadal variability characteristic of the North Pacific obscures’ attribution.

Data Availability Statement

465 Warnings of extreme swell in the Peruvian Coast were provided by the Directorate of Hydrography and Navigation (DIHIDRONAV) upon request. ERA5 reanalysis data are publicly available at <https://cds.climate.copernicus.eu>. The PDO index was obtained from NOAA (<https://www.ncei.noaa.gov/access/monitoring/pdo/> accessed, November 2025). The other climate indices used in this study are available from NOAA repositories at <https://psl.noaa.gov/data/climateindices/>. The codes used in this study are available from the corresponding author upon reasonable request.



470 **Author contributions**

GA contributed to conceptualization, formal analysis, investigation, software development, visualization, data curation, and writing of the original draft. SC contributed to conceptualization, formal analysis, software development, visualization, and writing of the original draft. RGH contributed to conceptualization, supervision, and writing—review and editing.

Competing interests

475 The authors declare that they have no conflict of interest.

Acknowledgements

The authors thank the many individuals and institutions that made this work possible. In particular, we acknowledge support from the Directorate of Hydrography and Navigation (DIHIDRONAV) from the Peruvian Navy, which provided detailed records of extreme swell events in the Southern Hemisphere, which guided this analysis. As well, we acknowledge the
480 European Centre for Medium-Range Weather Forecasts for producing the ERA5 reanalysis and making it freely accessible.

Financial support

SC was funded by the European Union's Horizon 2020 research and innovation program under the Marie Skłodowska-Curie grant agreement No 847635 (UNA4CAREER) through the SAFETE project (code 4230420).

References

- 485 Abram, N., Mulvaney, R., Vimeux, F. et al.: Evolution of the Southern Annular Mode during the past millennium. *Nature Clim Change* **4**, 564–569, <https://doi.org/10.1038/nclimate2235>, 2014
- Aguirre, C., Rutllant, J., Falvey, M.: Wind waves climatology of the Southeast Pacific Ocean. *Int. J. Climatology*, **37**(10), 4288–4301, <https://doi.org/10.1002/joc.5084>, 2017
- Alves, J. H. G. M.: Numerical modeling of ocean swell contributions to the global wind-wave climate, *Ocean Modelling*,
490 11(1–2), 98–122, <https://doi.org/10.1016/j.ocemod.2004.11.007>, 2006
- Ardhuin, F., Chapron, B., and Collard F.: Observation of swell dissipation across oceans, *Geophysical Research Letters*, **36**, L06607, <https://doi.org/10.1029/2008GL037030> , 2009
- Barber, N. F., and Ursell F.: The generation and propagation of ocean waves and swell. I. Wave periods and velocities, *Philosophical Transactions of the Royal Society of London. Series A, Mathematical and Physical Sciences*, **240**(824), 527–
495 560, <https://doi.org/10.1098/rsta.1948.0005>, 1948



- Barnston, A. G., Livezey, R. E.: Classification, seasonality and persistence of low-frequency atmospheric circulation patterns, *Monthly Weather Review*, **115**, 1083–1126, [https://doi.org/10.1175/1520-0493\(1987\)115<1083:CSAPOL>2.0.CO;2](https://doi.org/10.1175/1520-0493(1987)115<1083:CSAPOL>2.0.CO;2), 1987
- Barriopedro, D., Jiménez-Esteve B., Collazo S., Garrido-Perez J. M., Johnson J. E., and García-Herrera. R.: A multi-method attribution analysis of the Spain's 2024 extreme precipitation event. *Bull. Amer. Meteor. Soc.*, **106**, E2440–E2460, <https://doi.org/10.1175/BAMS-D-25-0049.1>, 2025
- Barriopedro, D., Ayarzagüena, B., García-Burgos, M., and García-Herrera, R.: A multi-parametric perspective of the North Atlantic eddy-driven jet. *Clim Dyn* **61**, 375–397. <https://doi.org/10.1007/s00382-022-06574-w>, 2023
- Boucharel, J., Santiago, L., Almar, R., and Kestenare, E.: Coastal wave extremes around the Pacific and their remote seasonal connection to climate modes. *Climate*, **9**(12), 168. <https://doi.org/10.3390/cli9120168>, 2021
- 505 Bukenberger, M., Fasnacht, L., Rüdüsühli, S., and Schemm, S.: A climatological characterization of North Atlantic winter jet streaks and their extremes, *Weather Clim. Dynam.* **6**, 279–316, <https://doi.org/10.5194/wcd-6-279-2025>, 2025
- Campos-Caba, R.V.: Análisis de marejadas históricas y recientes en las costas de Chile. Memoria de Título, Facultad de Ingeniería, Univ. de Valparaíso, Chile, 136 pp, 2016
- Cattiaux, J., Vautard R., Cassou C., You P., Masson-Delmotte V., and Codron F.: Winter 2010 in Europe: A cold extreme in
510 a warming climate. *Geophys. Res. Lett.*, **37** (20),1–6, <https://doi.org/10.1029/2010GL044613>, 2010
- Chen, D., and Sun, Q.: Northern Pacific extratropical cyclone variability and its linkage with Arctic sea ice changes, *Climate Dynamics*, **61**, 5875–5885, <https://doi.org/10.1007/s00382-023-06889-2>, 2023
- Collazo, S., García-Herrera. R., and Barriopedro, D.: Summer upper-level jets modulate the response of South American climate to ENSO. *Climate Dynamics*, **62**(3–4), 1031–1054. <https://doi.org/10.1007/s00382-023-06955-9>, 2024
- 515 Deng, K., Azorin-Molina, C., Minola, L., Zhang, G., Chen, D.: Global near-surface wind speed changes over the last decades revealed by reanalyses and CMIP6 model simulations, *Journal of Climate*, **34**, 2219–2234, <https://doi.org/10.1175/JCLI-D-20-0310.1>, 2021
- Directorate of Hydrography and Navigation: Avisos especiales. Available at: <https://www.dhn.mil.pe/portal/avisos-especiales> (accessed 12 November 2025), 2025
- 520 Dong, B., and Dai, A.: (2015), The influence of the Interdecadal Pacific Oscillation on temperature and precipitation over the globe, *Climate Dynamics*, **45**, 2667–2681, <https://doi.org/10.1007/s00382-015-2500-x>, 2015
- Fogt RL, and Marshall GJ.: The Southern Annular Mode: Variability, trends, and climate impacts across the Southern Hemisphere. *WIREs Clim Change*; **11**:e652. <https://doi.org/10.1002/wcc.652>, 2020
- García-Burgos, M., Ayarzagüena, B., Barriopedro, D., and García-Herrera, R.: Jet configurations leading to extreme winter temperatures over Europe. *Journal of Geophysical Research: Atmospheres*, **128**, e2023JD039304. <https://doi.org/10.1029/2023JD039304>, 2023
- 525



- Hell, M. C., Ardhuin F., Babanin A. C., and Queffeuilou P.: Swell generation under extra-tropical storms, *Journal of Geophysical Research: Oceans*, 126(11), e2021JC017637, <https://doi.org/10.1029/2021JC017637>, 2021
- 530 Henley, B. J.: Pacific decadal climate variability: Indices, patterns and tropical–extratropical interactions, *Global and Planetary Change*, **155**, 42–55, <https://doi.org/10.1016/j.gloplacha.2017.06.004>, 2017
- Hersbach, H., et al.: The ERA5 global reanalysis. *Quart. J. Roy. Meteorol. Soc.*, 146, 1999–2049. <https://doi.org/10.1002/qj.3803>, 2020
- Hsu, P.-C., Hsu, H.-H., Hong, H.-J., et al.: Subtropical warming enhances North Pacific midlatitude winter storm track activity in recent decades, *npj Climate and Atmospheric Science*, **8**, 235, <https://doi.org/10.1038/s41612-025-01108-7>, 2025
- 535 Infobae: Oleaje anómalo llegará a su punto pico este fin de semana en la costa peruana, advierte la Marina de Guerra (in Spanish), 27 May 2023. Available at: <https://www.infobae.com/peru/2023/05/27/oleaje-anomalo-llegara-a-su-punto-pico-este-fin-de-semana/> (accessed 12 November 2025), 2023
- King, J., Anchukaitis, K.J., Allen, K. et al.: Trends and variability in the Southern Annular Mode over the Common Era. *Nat Commun* **14**, 2324. <https://doi.org/10.1038/s41467-023-37643-1>, 2023
- 540 Lodise, J., Merrifield, S., Collins, C., Rogowski, P., Behrens, J., and Terrill, E.: Global climatology of extratropical cyclones from a new tracking approach and associated wave heights from satellite radar altimeter. *Journal of Geophysical Research: Oceans*, 127, e2022JC018925. <https://doi.org/10.1029/2022JC018925>, 2022
- Ma, X., Zhang, Y.: Interannual variability of the North Pacific winter storm track and its relationship with extratropical atmospheric circulation, *Climate Dynamics*, **51**, 3685–3698, <https://doi.org/10.1007/s00382-018-4104-8>, 2018
- 545 Mann, H.B., and Whitney, D.R.: On a test of whether one of two random variables is stochastically larger than the other. *Annals of Math. Statistics*, 18(1), 50–60. <https://doi.org/10.1214/aoms/1177730491>, 1947
- Marshall, G. J.: Trends in the Southern Annular Mode from Observations and Reanalyses. *J. Climate*, **16**, 4134–4143, [https://doi.org/10.1175/1520-0442\(2003\)016<4134:TITSAM>2.0.CO;2](https://doi.org/10.1175/1520-0442(2003)016<4134:TITSAM>2.0.CO;2), 2003
- 550 Purich, A., Arblaster, J. M., Boschat, G., et al.: Southern Annular Mode dynamics, projections and impacts in a changing climate, *Nature Reviews Earth & Environment*, <https://doi.org/10.1038/s43017-025-00746-y>, 2025
- RPP Noticias: Fuerte oleaje golpea a caletas y desembarcaderos del litoral norte peruano (in Spanish), Radio Programas del Perú, 27 December 2024. Available at: <https://rpp.pe/peru/actualidad/fuerte-oleaje-golpea-a-caletas-y-desembarcaderos-del-litoral-norte-peruano-video-noticia-1606850> (accessed 12 November 2025), 2024.
- Schultz, D. M., Keyser D., and Bosart L. F.: The effect of large-scale flow on the evolution of the occluded cyclone of 21–23 January 1997, *Bulletin of the American Meteorological Society*, 82(9), 1863–1891, [https://doi.org/10.1175/1520-0477\(2001\)082<1863:T_EOLFO>2.3.CO;2](https://doi.org/10.1175/1520-0477(2001)082<1863:T_EOLFO>2.3.CO;2), 2001
- Semedo, A., Weisse R., Behrens A., Günther H., Gulev S. K., and Sterl V.: A global view on the wind sea and swell climate and variability from ERA-40, *Journal of Climate*, 24(5), 1461–1479, <https://doi.org/10.1175/2010JCLI3718.1>, 2011



- Seneviratne, S. I., et al.: Chapter 11: Weather and climate extreme events in a changing climate. In *Climate Change 2021: The Physical Science Basis. Contribution of Working Group I to the Sixth Assessment Report of the Intergovernmental Panel on Climate Change* (pp. 1513–1766). Cambridge University Press. <https://doi.org/10.1017/9781009157896.013>, 2021
- Stewart, R.H.: Introduction to Physical Oceanography (Chapter 16: Ocean Waves). Open textbook, Texas A&M Univ. Available at: http://ocean.tamu.edu/Faculty/Stewart/intro_oc.html, 2008
- Tamayo Infantes, M.: Oleaje anómalo de fuerte intensidad en la bahía de Miraflores, *Bitácora Hidrográfica*, 3, 13–16, Dirección de Hidrografía y Navegación de la Marina de Guerra del Perú, Lima, Peru. Available at: https://www.dhn.mil.pe/Archivos/bitacora/edc_03.pdf, 2007
- Virtanen, P., Gommers R., Oliphant T. E., Haberland M., Reddy T., Cournapeau D., Burovski E., Peterson P., Weckesser W., Bright J., et al.: SciPy 1.0: Fundamental algorithms for scientific computing in Python, *Nature Methods*, 17(3), 261–272, <https://doi.org/10.1038/s41592-019-0686-2>, 2020
- Wallace, J. M., Gutzler, D. S.: Teleconnections in the geopotential height field during the Northern Hemisphere winter, *Monthly Weather Review*, **109**, 784–812, [https://doi.org/10.1175/1520-0493\(1981\)109<0784:TITGHF>2.0.CO;2](https://doi.org/10.1175/1520-0493(1981)109<0784:TITGHF>2.0.CO;2), 1981
- Wang, X., and Yang, X.-Q.: Amplified asymmetric impact of ENSO events on the wintertime Pacific–North American teleconnection pattern, *Geophysical Research Letters*, **50**, e2022GL100996, <https://doi.org/10.1029/2022GL100996>, 2023
- Wills, R. C. J., Battisti, D. S., Proistosescu, C., Thompson, L., Hartmann, D. L., and Armour, K.: Ocean circulation signatures of North Pacific decadal variability. *Geophysical Research Letters*, 46, 1690–1701. <https://doi.org/10.1029/2018GL080716>, 2019
- Xu, G., Broadman, E., Dorado-Liñán, I. et al.: Jet stream controls on European climate and agriculture since 1300 ce. *Nature* **634**, 600–608, <https://doi.org/10.1038/s41586-024-07985-x>, 2024
- Yiou, P., Jézéquel A., Naveau P., Otto F. E. L., Vautard R., and Vrac M.: A statistical framework for conditional extreme event attribution. *Adv. Stat. Climatol. Meteor. Oceanogr.*, 3 (1), 17– 31, <https://doi.org/10.5194/ascmo-3-17-2017>, 2017